POI-associated LMD-3 mutation impairs B12-regulated lysosomal function and reproductive capacity in *C. elegans*

Yile Zhai[1*], Tiantian Wang[2*], Meixi Gong[2], Wenfei Li[2#], Xin Wang[3#], Zhe Zhang[1,2#]

[1]Institute of Medical Sciences, the Second Hospital, Cheeloo College of Medicine, Shandong University, Jinan, Shandong, China.

[2]Department of Histology and Embryology, School of Basic Medical Sciences, Cheeloo College of Medicine, Shandong University, Jinan, Shandong, China.

[3]State Key Laboratory for Conservation and Utilization of Bio-Resources in Yunnan, Yunnan University, Kunming, Yunnan, China.

*These authors contributed equally: Yile Zhai, Tiantian Wang.

[#]Correspondence: wenfeili@sdu.edu.cn (W. Li), xinwang2@ynu.edu.cn (X. Wang), zhezhang@sdu.edu.cn (Z. Zhang)

Abstract

Reproductive longevity decline is a key feature of aging and premature ovarian insufficiency (POI). While proteostasis collapse is implicated in reproductive aging, the molecular link remains elusive. Here, we engineered the clinically relevant W690C mutation into *C. elegans lmd-3* gene, the human *NCOA7* ortholog, to establish a valuable in vivo POI model. The mutation severely compromises LMD-3 protein stability and expression, leading to a profound collapse in reproductive capacity driven by germline apoptosis. We demonstrate that this defect drives catastrophic autophagic-lysosomal dysfunction, blocking degradation and causing proteotoxic accumulation of misfolded proteins. Crucially, we define this pathology as a functional B12 deficiency and show that mecobalamin (meCbl) supplementation successfully restores proteostasis. Together, these findings delineate a conserved genetic pathway from LMD-3 destabilization to reproductive failure and propose vitamin B12 as a readily translatable therapeutic intervention for age-related reproductive decline.

Introduction

Reproductive longevity is fundamental for female fertility and healthy aging, yet its decline is one of the first biological processes to emerge in many organisms, from *C. elegans* to humans[1,2]. In humans, the ovary is uniquely susceptible, with its function diminishing decades before other somatic systems[3,4]. This early and pronounced decline contributes significantly to age-related infertility and premature ovarian insufficiency (POI), posing a major global health challenge[1,5]. A growing body of evidence links this decline to impaired proteostasis, the cellular network that maintains protein quality control[6]. While cellular stress responses and protein quality control systems are evolutionarily shared across species[7-9], the specific molecular pathways that connect these processes to reproductive failure remain elusive.

The nematode *C. elegans* provides a powerful and evolutionarily conserved model for investigating reproductive aging[10,11]. Its distinct and early decline in fertility mirrors the human condition, making it an ideal platform to dissect the molecular basis of reproductive health[2,12]. This decline is largely driven by a loss of germline integrity and function, which is highly dependent on the maintenance of a healthy proteome, a process regulated by conserved cellular systems, including the lysosomal and autophagic pathways[13-15].

The oxidation resistance 1 (OXR1) protein family is a key player in this process, comprised of OXR1 and nuclear receptor coactivator 7 (NCOA7) in mammals[16]. This evolutionarily conserved family acts as a critical protective mechanism against cellular

stress[17,18]. NCOA7 has recently been identified as a key regulator of ovarian longevity in humans and mice, and its orthologs have been shown to protect against oxidative damage in other species like *C. elegans* and zebrafish[19-21]. The TLDc domain of these proteins is known to directly interact with the V-type ATPase, a proton pump essential for lysosomal acidification and degradative function[22,23]. This shared function and evolutionary conservation highlight the potential of using *C. elegans* model to gain insights into human disease.

In this study, we engineered a clinically relevant human mutation in *C. elegans* to investigate the pathogenic mechanism of POI. We created the W690C single-point mutation in the conserved TLDc domain of *C. elegans* LMD-3, which perfectly corresponds to a pathogenic NOCA7^{W804C} mutation found in human patients with POI[19]. We demonstrate that this single-point mutation significantly impairs reproductive capacity, causing reduced germline cell numbers and increased apoptosis. Mechanistically, our findings reveal that the mutation severely compromises LMD-3 protein stability and gene expression, leading to profound cellular autophagic-lysosomal dysfunction. This defect impairs both lysosomal acidification and its degradative capacity, causing the widespread accumulation of misfolded proteins and aggregates in the germline.

Critically, we show that this defect results in a functional B12 deficiency that can be corrected by mecobalamin (meCbl) supplementation, thereby restoring proteostasis. These findings provide critical insights into the molecular basis of female reproductive longevity, establishing a valuable genetic model for studying POI and highlighting a

potential therapeutic target for mitigating age-related reproductive decline.

Results

Genetic and structural evidence for a shared POI-associated W690C mutation in LMD-3

The *C. elegans* LMD-3 protein, which serves as the sole OXR1 family member in the nematode, possesses a domain architecture highly conserved with its human orthologs, OXR1 and NCOA7 (Fig. 1A). This architecture is defined by three highly conserved LysM, GRAM, and TLDc domains. Despite the low 26.46% overall amino acid sequence identity between LMD-3 and human NCOA7[24], the key functional domains, including the TLDc domain and other conserved motifs, are remarkably homologous (Supplementary Fig. 1).

The conservation of these domains is further highlighted by the POI-associated tryptophan residue (W804) in the TLDc domain of human NCOA7[19]. This residue is perfectly conserved across multiple species, including the corresponding W690 residue in *C. elegans* LMD-3 (Fig. 1B and Supplementary Fig. 1)[25]. The remarkable conservation of this clinically relevant residue across species provides a strong genetic basis for a shared pathogenic mechanism and validates the use of *C. elegans* W690C mutant as a model for human POI.

Following strong genetic evidence for a shared mechanism, we next sought to determine if this functional similarity was underpinned by structural conservation. A

79 comparative structural analysis using AlphaFold3 revealed a remarkable similarity
80 between the predicted *C. elegans* LMD-3 structure and its human NCOA7 ortholog
81 (Fig. 1C). Despite differences in unique α-helices and intrinsic disordered regions
82 (IDRs), the core LysM, GRAM, and TLDc domains were highly conserved. This
83 structural homology was particularly striking in the V-ATPase-interacting TLDc domain,
84 which showed an almost identical conformation and the conserved W804/W690 site
85 (Fig. 1C and Supplementary Movie 1). These results provide compelling structural
86 evidence that the TLDc-V-ATPase interaction is a central, conserved mechanism
87 governing lysosomal activity and proteostasis across species.

88 Based on this strong evidence for a shared mechanism, we created an in vivo
89 model of human POI by introducing the orthologous W690C mutation into *C. elegans*
90 *lmd-3* using CRISPR/Cas9 (Fig. 1D and supplementary Table 1). A preliminary analysis
91 of the *lmd-3*^{W690C} homozygous mutant animals revealed no obvious developmental
92 defects, as confirmed by a lack of significant difference in body length compared to
93 wild-type animals (Fig. 1F, G). The lack of significant developmental defects, consistent
94 with the primary reproductive phenotype observed in human POI[19], establishes the
95 *lmd-3*^{W690C} strain as a high-fidelity in vivo model for investigating the molecular
96 mechanisms of this disease.

97

98 **The POI-associated W690C mutation impairs fecundity and germline integrity in**
99 ***C. elegans***

The deleterious W804C mutation in human NCOA7 has been shown to contribute to POI by accelerating oxidative stress-induced cellular senescence in ovarian granulosa cells[19]. Given the perfect conservation of this residue in *C. elegans* LMD-3 and the established role of this protein in oxidative stress resistance[20,26], we investigated whether the orthologous *lmd-3*^{W690C} mutation would impair reproductive capacity in a manner consistent with the human disease. Our results showed a pronounced defect in fecundity, with the mutant strain exhibiting a 32.1% reduction in total progeny over their lifespan compared to wild-type animals (Fig. 2A and Supplementary Fig. 2A, B). Mirroring the rapid decline in fertility observed in human POI, this reduction was particularly striking during the peak reproductive period, suggesting that the mutation causes an accelerated and severe decline in fertility.

To understand the cellular basis for this reduced fecundity, we next assessed germline integrity, hypothesizing that the pronounced reduction in fecundity was a direct result of germ cell deficiency[27]. The *C. elegans* germline is a dynamic, spatially organized tissue that produces all progeny. It is divided into distinct zones of proliferation, meiosis, and differentiation, all of which are essential for producing viable offspring (Fig. 2B). Germ cells are maintained by a distal stem cell region, regulated by the distal tip cell (DTC), which allows for clear visualization and analysis of germ cell progression throughout the gonad[28].

Quantitative analysis of DAPI-stained gonads confirmed a significant reduction in the total number of germ cells in Day 1 adult *lmd-3*^{W690C} mutants (Fig. 2C, D). This defect was accompanied by a specific decline in the number of proliferative germline

122 stem cells (Fig. 2E), indicating that the *lmd-3*^{W690C} mutation fundamentally
123 compromises the maintenance of the germline progenitor pool, which is essential for
124 ongoing germ cell production and homeostasis[29].

125 To investigate the mechanism driving germ cell loss, we assessed germline
126 apoptosis, a process frequently linked to oxidative stress[30]. Using two complementary
127 methods, the nucleic acid dye SYTO12 and a *lim-7*p::*ced-1*::GFP reporter[31,32], we
128 observed a significant increase in apoptotic cell corpses within the germline of W690C
129 mutants at Day1 and Day2 of adulthood (Fig. 2F, G and Supplementary Fig. 2C, D).
130 The finding directly links increased germ cell death to reduced fecundity in this POI
131 model. Our results collectively demonstrate the *lmd-3*^{W690C} mutation compromises
132 germline integrity and reproductive capacity by promoting apoptosis, validating the
133 mutant as a valuable in vivo model for human POI.

134

135 **The LMD-3 W690C mutation induces widespread and chronic cellular stress**

136 To gain a deeper understanding of the physiological role of LMD-3, we first
137 characterized its expression and subcellular localization. An integrated (Is)
138 transcriptional reporter revealed that *lmd-3* is broadly expressed, including the nervous
139 system, intestine, and vulva (Fig. 3A)[26]. Subcellular fractionation of the N-terminal
140 mCherry-tagged LMD-3 protein and its TLDc domain confirmed their predominant
141 localization to the cytoplasm and membrane fractions (Fig. 3B), consistent with its
142 known association with lysosomes and the V-ATPase complex[22,23]. A minor nuclear

143 fraction was also observed, which aligns with the transcriptional and antioxidant
144 functions of its orthologs NCOA7 and OXR1 (Fig. 3B)[33,34].

145 Based on the established link between oxidative stress-induced cellular
146 senescence and POI[19], and given that the LMD-3 orthologs in yeast and humans are
147 known to be stress-inducible[26,35], we hypothesized that LMD-3 expression would
148 increase with age as a protective response. Indeed, we found a gradual, age-
149 dependent increase in *lmd-3* transcription (Fig. 3C, D), a pattern suggesting that LMD-
150 3 is actively involved in preserving cellular health and longevity as the organism ages.
151 This finding further supports a conserved role for LMD-3 as a protective factor against
152 age-related stress, thereby promoting survival.

153 To determine if the W690C mutation compromises cellular stress resilience, we
154 monitored cytoplasmic and endoplasmic reticulum (ER) stress throughout the late larval
155 and early adult stages. We found that the cytosolic unfolded protein response (UPR^{cyto}),
156 monitored by the *hsp-16.2*p::GFP reporter[36], showed a gradual but dramatic induction
157 in the mutants (Fig. 3E, F and Supplementary Table 2), indicating an increase in
158 oxidative stress. In parallel, the ER unfolded protein response (UPR^{ER}), as indicated
159 by the increased expression of the *hsp-4*p::GFP reporter[37], also showed a progressive
160 but apparent activation (Fig. 3G, H and Supplementary Table 2).

161 These results show that the POI-associated W690C mutation induces widespread
162 but relatively mild and chronic cellular stress, as evidenced by the activation of both
163 cytosolic and ER stress pathways. However, this general stress response is not

164 sufficient to fully account for the early and severe reproductive decline observed in the
165 mutant. This discrepancy suggests that the reproductive failure is not a secondary
166 consequence of this general chronic stress but rather stems from a direct and severe
167 breakdown in essential germline protein quality control, specifically through impaired
168 lysosomal function and protein degradation[6,19,38].

169

170 **The W690C-induced lysosomal dysfunction drives proteostasis collapse**

171 Building on the established interaction between the TLDc domain and V-ATPases[22,23],
172 and the central role of lysosomes in aging, we investigated the impact of the W690C
173 mutation on lysosomal function. Our transcriptional analysis revealed a significant
174 downregulation of a wide range of lysosome-related genes in the mutant (Fig. 4A and
175 Supplementary Fig. 3A). This included key components for acidification (V-ATPases),
176 lysosomal structural integrity (LMP-2, NCR-1), and degradation (cathepsin proteases
177 ASP-3, ASP-4). The initial finding suggests that the W690C mutation severely impairs
178 the biogenesis and overall function of the lysosomal system.

179 To directly confirm that the transcriptional defects led to a loss of lysosomal
180 function, we measured lysosomal acidification, a process critical for protein
181 degradation[39]. The use of a heat-shock-inducible pH-sensitive reporter, NUC-
182 1::pHTomato[40], revealed a significantly higher fluorescence intensity in the mutant,
183 indicating a less acidic, more neutralized lysosomal pH (Fig. 4B, C and Supplementary
184 Fig. 3B, C). This defect was independently corroborated by co-staining with the

185 acidotropic dye LysoSensor Green (LSG) and the lysosome-specific dye LysoTracker
186 Red (LTR)[41]. The resulting reduced LSG/LTR fluorescence ratio in the mutant
187 definitively confirmed that the transcriptional defects resulted in a severe impairment
188 of lysosomal acidity in *C. elegans* (Fig. 4D, E and Supplementary Fig. 3D, E).

189 The consequence of the acidification defect was a severe breakdown in
190 degradative capacity, which we assessed by monitoring the clearance of secreted
191 ssGFP[42]. The reporter showed a significant accumulation of fluorescence in the
192 coelomocytes of the mutant (Fig. 4F, G), demonstrating a failure of lysosomal
193 degradation. This defective degradation led to a broad collapse in proteostasis, as
194 evidenced by extensive aggregation of the age-related protein NMY-2::GFP in
195 oocytes[43] (Fig. 4H) and the polyglutamine reporter Q40::YFP in body wall muscles[44]
196 (Fig. 4I). The vital role of LMD-3 in protein homeostasis was further highlighted by the
197 accumulation of vitellogenin, a major egg yolk protein, in the mutant's intestine,
198 pseudocoelom, and germline (Supplementary Fig. 3F), confirming that LMD-3
199 deficiency impairs the processing of this crucial reproductive protein.

200 To establish that the lysosomal defect is a direct cause of the reproductive failure,
201 we used the *vha-12(ok821)* mutant to genetically neutralize V-ATPase activity. This
202 loss-of-function allele not only recapitulated the reproductive defects observed in the
203 W690C mutant but also exacerbated the decline (Supplementary Fig. 3G). These
204 findings cement a causal link between the W690C-induced V-ATPase dysfunction and
205 reproductive decline, underscoring the vital role of LMD-3 in maintaining lysosomal
206 function for reproductive longevity.

207

208 **Vitamin B12 restores proteostasis by repairing LMD-3(W690C)-mediated**
209 **autophagic-lysosomal defects**

210 Following our discovery of profound lysosomal dysfunction and proteostasis collapse
211 in the LMD-3(W690C) mutant, which mirrors the defective autophagy and senescence
212 linked to NCOA7 dysfunction in human POI[19], we investigated the integrity of the
213 autophagic pathway. We first utilized a transcriptional reporter for the stress-inducible
214 autophagy gene, *tts-1*[45]. In contrast to wild-type animals, the W690C mutants showed
215 a significant reduction in *tts-1*p::GFP fluorescence (Fig. 5A). This was further
216 supported by the notable downregulation of key autophagy genes, including the master
217 transcription factor *hlh-30*[46], along with genes essential for autophagosome formation,
218 cargo recognition, fusion, and lysosomal degradation (Fig. 5B, Supplementary Fig. 5A).
219 These findings suggested that the W690C mutation severely compromises the
220 biogenesis and overall function of the autophagic system.

221 To confirm that this transcriptional defect leads to a functional impairment, we
222 proceeded to examine the accumulation of SQST-1, the *C. elegans* ortholog of p62.
223 Efficient clearance of SQST-1 is indicative of a healthy autophagic flux, and we
224 observed a massive accumulation of SQST-1::GFP aggregates in the adult W690C
225 mutants (Fig. 5C and Supplementary Fig. 4B), providing strong evidence that the
226 overall autophagic degradation pathway is severely compromised.

227 To precisely characterize autophagic failure, we first utilized tandem fluorescent

228 reporter mCherry::GFP::LGG-1 to distinguish between autophagosomes formation
229 (yellow puncta) and maturation into autolysosomes (red puncta), where acid-sensitive
230 GFP is quenched in the acidic lysosomal environment[47]. Confocal analysis revealed a
231 dramatic increase in yellow puncta and a parallel decrease in red puncta in the W690C
232 mutant (Fig. 5D, E and Supplementary Fig. 4C, D). This block in autophagic flux at the
233 fusion/degradation stage directly reinforces the severe lysosomal acidification defect
234 observed previously (Fig. 4B-E). Furthermore, GFP::LGG-1 Western blot analysis
235 revealed a simultaneous defect in autophagosome biogenesis[48], shown by the
236 significant drop in the ratio of membrane-associated LGG-1-II (lipidated) to cytosolic
237 LGG-1-I (unlipidated) (Fig. 5F). These findings confirm the W690C mutation induces a
238 comprehensive, multi-stage failure of the autophagic-lysosomal pathway.

239 Given that LMD-3^{W690C} dysfunction impairs lysosomal function and reproductive
240 health, we hypothesized that enhancing cellular resilience could restore proper
241 lysosomal function. Since lysosomes are critical for the uptake and processing of
242 dietary vitamin B12, the catastrophic lysosomal failure in *lmd-3* mutants would result
243 in a state of functional B12 deficiency[49]. We therefore tested the capacity of the active
244 form, meCbl, to mitigate this lysosomal dysfunction. meCbl supplementation
245 significantly rescued the accumulation of the aggregation-prone protein NMY-2::GFP
246 in the germline (Fig. 5G, H) and improved protein clearance in coelomocytes, as
247 evidenced by reduced ssGFP fluorescence (Supplementary Fig. 4E, F). Collectively,
248 these results demonstrate that B12 supplementation mitigates cellular stresses and
249 directly improves the defective lysosomal function, thereby restoring germline

250 proteostasis and protein clearance in *lmd-3*^{W690C} mutants.

251

252 **The W690C mutation compromises LMD-3 structure and expression**

253 Having demonstrated the essential role of the W690C mutation in disrupting lysosomal
254 function and cellular homeostasis in *C. elegans*, we set out to determine the precise
255 molecular basis of this effect. We first investigated whether the mutation affected LMD-
256 3 expression at the transcriptional level. Using primers designed to target three distinct
257 locations along the gene (Fig. 6A and supplementary Table 3), we detected a
258 significant and consistent reduction in the overall *lmd-3* transcript level in the mutant
259 strain compared to the wild type (Fig. 6B and Supplementary Fig. 5A). This reduction
260 in transcript levels exacerbates the loss-of-function phenotype.

261 With the established link between human POI-associated NCOA7 mutations and
262 protein stability[19], we reasoned that the W690C mutation would compromise the
263 structure of LMD-3. To confirm this hypothesis, three-dimensional structural models of
264 the *C. elegans* wild-type and W690C-mutated LMD-3 protein were developed[50]. Our
265 model showed that the LMD-3 protein, like its human ortholog NCOA7, forms a
266 conserved trimer-like region comprised of its LysM, GRAM, and TLDc domains (Fig.
267 6C). Although the overall core domains maintained their general conformation, we
268 found that the W690C mutation significantly altered the inter-subunit distances within
269 the predicted trimer-like region (Fig. 6D). This structural change suggests a
270 destabilization of a key binding interface. Critically, six machine learning-based

methods confirmed that the W690C mutation leads to a compromise in overall protein stability (supplementary Table 4)[51-55], consistent with findings from a human study[19].

To directly confirm that the W690C mutation results in reduced protein stability, we performed a cycloheximide (CHX) chase assay to evaluate the turnover of LMD-3 protein[56]. As a result, while wild-type LMD-3 protein remained relatively stable, the mutant protein exhibited a significant decrease in levels, showing a marked degradation after 12 hours of CHX treatment (Fig. 6E, F and Supplementary Fig. 5B). This result provides compelling evidence that the W690C mutation compromises the stability of LMD-3 protein, mechanistically linking the structural defect to its rapid degradation. Collectively, these findings establish that the POI-associated W690C mutation compromises both *lmd-3* gene expression and protein stability, thereby leading to the lysosomal defects and reproductive decline.

Discussion

Reproductive longevity is a fundamental aspect of healthy aging, yet its molecular mechanisms remain incompletely understood. Our study establishes a novel POI-associated *C. elegans* model to dissect the pathophysiological basis underlying fertility decline. By introducing an orthologous W690C mutation into LMD-3, the single-gene family member of human NCOA7 and OXR1, we found compelling evidence that this genetic lesion impairs reproductive capacity by compromising protein stability and inducing a profound collapse in cellular proteostasis. These findings define a specific pathogenic mechanism in which a single amino acid substitution leads to widespread

293 cellular dysfunction, thereby directly linking a conserved protein to the maintenance of
294 reproductive health.

295 Our study reveals that the W690C mutation, located within the conserved TLDc
296 domain, severely compromises LMD-3 protein stability. This finding provides a crucial
297 mechanistic link between the genetic mutation and the observed loss-of-function
298 phenotypes. A key insight from our data is that this mutation also severely reduces the
299 overall *lmd-3* mRNA level (Fig. 6B), which directly contributes to the loss-of-function
300 phenotype. This observation contrasts sharply with the human NCOA7^{W804C} mutation,
301 where mRNA levels are unaffected[19]. This observed discrepancy in mRNA levels is a
302 critical point that highlights the mechanistic advantage of studying a non-redundant
303 system. In mammals, the presence of the ortholog OXR1 likely provides cellular
304 buffering or compensation that masks any regulatory feedback related to NCOA7 loss.
305 As *lmd-3* is the sole member of this gene family in *C. elegans*, its dysfunction has a
306 more direct, non-redundant, and severe impact, making our model an ideal system to
307 study the core pathogenic mechanism.

308 The destabilization of LMD-3^{W690C} protein leads to profound lysosomal dysfunction,
309 characterized by defective acidification and impaired degradative capacity. These data
310 align with emerging evidence that lysosomes are not merely "waste disposal plants"
311 but critical signaling hubs whose dysfunction is linked to aging and neurodegenerative
312 diseases[57-59]. Our study now unequivocally links organelle failure to a major defect in
313 reproductive capacity, thereby establishing a direct causal link. This primary lysosomal
314 defect triggers a downstream cascade of cellular damage, as the accumulation of

315 misfolded proteins and aggregates creates a proteotoxic environment that is
316 detrimental to sensitive, non-dividing cells like oocytes[6,60]. Such chronic cellular stress
317 eventually manifests as increased germ cell apoptosis and a reduction in total cell
318 number, fully accounting for the decline in reproductive capacity in the mutant.
319 Ultimately, our findings reveal an elegant pathway linking impaired proteostasis, a well-
320 known hallmark of aging[61], to the specific context of ovarian aging.

321 Beyond identifying the pathogenic mechanism, our study provides pioneering
322 evidence for a therapeutic strategy targeting this conserved pathway. Given that
323 lysosomal failure compromises the cellular uptake and processing of vitamin B12, the
324 LMD-3^{W690C} mutation creates a state of functional B12 deficiency that subsequently
325 disrupts propionate metabolism. This is critical because B12 is an essential cofactor
326 for the enzyme methylmalonyl-CoA mutase, which catalyzes a required step in
327 propionate metabolism[62]. A functional deficiency in meCbl impairs this pathway, which
328 is known to lead to toxic metabolite accumulation and cellular stress, thereby
329 exacerbating the lysosomal dysfunction[63]. Supplementation with the active form,
330 meCbl, successfully rescued the LMD-3^{W690C}-induced proteostasis collapse, directly
331 restoring germline protein homeostasis and enhancing clearance. This highly
332 significant finding suggests a simple nutritional supplement could mitigate the effects
333 of this severe genetic dysfunction, highlighting the immediate clinical relevance of our
334 *C. elegans* model.

335 Our human disease-driven *C. elegans* model represents a significant
336 advancement in the study of reproductive aging. By establishing a direct causal link

337 between a specific genetic lesion, lysosomal dysfunction, proteotoxicity, and
338 reproductive failure, our model moves beyond correlational studies. Furthermore, the
339 model is highly relevant to human POI, as it recapitulates key features of the human
340 condition, including germ cell depletion and premature reproductive decline[64].

341 Beyond the specific W690C mutation, our work suggests that LMD-3/NCOA7 and
342 its genetic interactors are promising candidates for genetic screening in patients with
343 idiopathic POI. Furthermore, our findings raise broader questions about the role of wild-
344 type LMD-3/NCOA7 in age-related fertility decline. Recent evidence has shown that
345 the expression and function of this protein naturally wane with age, leading to a gradual
346 decline in the lysosomal and proteostasis health observed in aged oocytes[19].
347 Consequently, our mutant model serves as an accelerated version of the natural aging
348 process, providing a powerful system for dissecting these fundamental mechanisms.

349 The *C. elegans* model we established provides an invaluable high-throughput in
350 vivo platform for screening potential drug interventions that can enhance lysosomal
351 activity through mechanisms like TFEB activation or other protein homeostasis-
352 restoring pathways like autophagy and proteostasis[47,65,66]. Furthermore, while our
353 study establishes LMD-3 as a crucial regulator of lysosomal activity, its precise
354 biochemical function within this organelle remains to be fully elucidated. Therefore,
355 further studies are required to identify its binding partners and determine whether it
356 acts as a scaffold, a regulator, or serves another function in maintaining lysosomal pH
357 and enzymatic activity.

358 In summary our study establishes that the POI-associated W690C mutation in
359 LMD-3, supported by genetic and structural evidence, compromises protein stability
360 and expression, leading to a profound collapse in lysosomal function. This collapse
361 triggers proteotoxic stress, germ cell death, and reproductive failure. Crucially, we
362 define the resultant phenotype as a functional B12 deficiency, rationalizing
363 mecobalamin supplementation as a viable therapeutic strategy. This discovery
364 provides a valuable in vivo platform for screening potential therapeutic compounds.
365 Furthermore, it establishes lysosomal activity as a crucial determinant of reproductive
366 longevity and a promising target for extending reproductive capacity.

367

368 **Methods**

369 ***C. elegans* strains and maintenance**

370 We maintained all *C. elegans* strains (Supplementary Table 1), including the wild-type
371 N2 Bristol strain and all other strains, at 20°C on standard nematode growth medium
372 (NGM) plates. These plates were uniformly seeded with *Escherichia coli* OP50 as a
373 food source. To ensure experimental synchrony, we obtained age-matched
374 populations by treating gravid adults with a bleaching solution to isolate and hatch eggs.

375

376 **CRISPR-Cas9 mediated mutagenesis**

377 The *lmd-3*^{W690C} point mutation was generated by SunyBiotech using the established

378 CRISPR-Cas9 gene editing system. The presence of the desired point mutation was
379 then definitively confirmed by Sanger sequencing (Supplementary Table 3). To remove
380 any potential off-target mutations and ensure a clean genetic background, the verified
381 mutant was subsequently outcrossed to the wild-type N2 strain three times before all
382 phenotypic and functional analyses commenced.

383

384 **Plasmid construction**

385 To facilitate biochemical analyses in mammalian cells, we generated expression
386 vectors for 1xFLAG-tagged LMD-3 proteins. The full-length *lmd-3* cDNA sequence
387 were amplified by PCR from both the wild-type and *lmd-3*^{W690C} mutant strains. These
388 amplified fragments were subsequently subcloned into the pcDNA3.1 vector. Primers
389 used for the amplification are listed (Supplementary Table 3).

390

391 **Quantitative real-time PCR (qRT-PCR)**

392 To quantify target gene transcripts, 200 synchronized Day 1 adult animals were
393 collected into M9 buffer, lysed using Trizol Reagent (Invitrogen, 15596026CN), and
394 immediately frozen in liquid nitrogen. Total RNA was subsequently isolated via
395 standard chloroform extraction and isopropanol precipitation. A total of 1.2 μg isolated
396 RNA was then reverse-transcribed into complementary DNA (cDNA) using the HiScript
397 III 1st Stand cDNA Synthesis Kit (+ gDNA wiper) (Vazyme, R312-01). Quantitative real-
398 time PCR (qRT-PCR) was performed on an ABI QuantStudio 1 machine using ChamQ

399 SYBR Color qPCR Master Mix (Vazyme, Q411-02). Transcript levels for the target
400 genes were calculated and normalized to the endogenous control gene, *act−1*.

401

402 **Reproductive span analysis**

403 As previously described, a minimum of 10 synchronized hermaphrodite larvae at L4
404 stage for each strain were individually transferred to fresh NGM plates at every 12
405 hours[67]. This transfer process continued until the cessation of reproduction, allowing
406 for the isolation of all laid eggs. The number of progenies was counted at each transfer,
407 and the total number of progenies per animal was calculated. The experiment was
408 performed in three biological replicates.

409

410 **Measurement of body length**

411 Synchronized *C. elegans* at designated developmental stages were first anesthetized
412 using levamisole and mounted onto agarose pads. Images were captured using a
413 Nexcope 910 microscopy system. The linear distance from the head to the tail of each
414 worm was then measured using the Image View software to determine body length. A
415 minimum of 22 worms were analyzed for each group.

416

417 **Microscopy and imaging analysis**

418 For all standard fluorescence and bright-field microscopy experiments, synchronized

419 animals were first anesthetized using levamisole and mounted onto agarose pads for
420 imaging. Images were captured using either a Nexcope 910 fluorescence microscope
421 or a high-resolution laser scanning confocal microscope (Carl Zeiss, LSM 980),
422 depending on the required resolution and image type. Subsequently, fluorescence
423 intensity and other quantitative metrics, such as puncta number or size, were
424 measured and analyzed using the ImageJ software package.

425

426 **Germline staining and quantification**

427 To analyze the integrity and morphology of the germline, synchronized Day 1 adult
428 animals were first fixed by immersion in ice-cold methanol for 5 minutes. Following the
429 removal of methanol, the samples were washed three times with M9 buffer. Germ cell
430 nuclei were then stained by incubating the samples in a DAPI solution (Macklin,
431 D807022) for 30 minutes in the dark, followed by three additional washes. The stained
432 worms were then mounted, and their gonads were examined using a laser scanning
433 confocal microscope. The total number of germ cells and the specific count of
434 proliferative germline stem cells in each gonad were subsequently determined
435 quantitatively using ImageJ software.

436

437 **SYTO12 staining for germline apoptotic cells**

438 Synchronized larvae from control and experimental groups were collected and allowed
439 to develop into Day 1 and Day 2 adults. These adult animals were then stained by

440 incubation in SYTO 12 dye (Thermo Fisher Scientific, S7575) in the dark for 3 hours.
441 Following staining, worms were washed three times with buffer via centrifugation
442 (4,000 rpm, 1 minute) and transferred to fresh NGM plates for a 1-hour recovery period
443 to clear dye-labeled bacteria from the intestines. Finally, the worms were anesthetized
444 with levamisole, mounted on agarose pads, and imaged using an objective under
445 green fluorescence microscopy to count the apoptotic cell corpses.

446

447 **Dual lysosomal staining and quantification**

448 Synchronized Day 1 adult animals were co-stained for 1 hour at 20°C in the dark with
449 10 mM LysoSensor Green DND-189 (Yeasen) and LysoTracker Red DND-99 (Yeasen),
450 as previously described[68]. The animals were transferred to fresh NGM plates seeded
451 with OP50 for a 1-hour recovery period to clear residual dye from the gut bacteria.
452 Lysosomal acidification was then quantitatively evaluated by measuring the relative
453 fluorescence intensity ratio of LysoSensor Green to LysoTracker Red using ImageJ
454 software, where a lower ratio indicates reduced lysosomal acidity.

455

456 **Cell culture and Transient transfection**

457 HEK-293T cells were maintained in Dulbecco's Modified Eagle's Medium (DMEM)
458 (Gibco, C119955-00BT) supplemented with 10% fetal bovine serum (FBS) (Excell,
459 FSP-500) in a humidified atmosphere at 37°C with 5% CO_2. For transient transfection
460 experiments, cells were transfected with the appropriate plasmid DNA using

461 polyethyleneimine (PEI) (Sigma-Aldrich, 408727). The transfection mixture was
462 prepared using a DNA-to-PEI mass ratio of 1:4.5, with a total of 1 μg DNA per 10^6
463 cells used for each condition.

464

465 **Cycloheximide pulse chase assay**

466 The compromised stability of the 1xFLAG-tagged protein was evaluated in cells using
467 a Cycloheximide (CHX) chase assay, which monitors protein turnover[69]. Thirty-six
468 hours after transfection, cells were subjected to 50 μg/mL CHX to block protein
469 synthesis. At designated time points, cells were collected, and the degradation of wild-
470 type and mutant were determined by quantifying protein levels via Western blotting.

471

472 **Autophagy flux and aggregation analysis**

473 To assess autophagy flux, synchronized worms expressing the tandem fluorescent
474 reporter mCherry::GFP::LGG-1 were used. Puncta were counted in the anterior
475 intestinal cells, where the number of autophagosomes (AP) was determined by
476 counting the puncta positive for both the GFP and mCherry (yellow/orange), and the
477 number of autolysosomes (AL) was determined by counting mCherry-only positive
478 puncta (red, due to quenching in the acidic lysosome). Additionally, to evaluate the
479 accumulation of aggregated cargo, the number of SQST-1::GFP positive puncta was
480 counted specifically within the head neurons of synchronized worms. Both assays
481 were conducted with a minimum of 11 worms examined per condition across three

482 independent experiments.

483

484 **Mecobalamin supplementation**

485 A 150 μM stock solution of meCbl (Macklin, M812748) was initially prepared in H_2O
486 (which also served as the control solvent). This stock solution was then diluted to a
487 final working concentration of 0.15 μM directly into the NGM agar prior to pouring the
488 plates, ensuring the worms were exposed to the compound throughout their life cycle.

489

490 **Quantification of *myo-3*p::ssGFP intensity**

491 Fluorescence images were captured from synchronized adult *C. elegans* at Day 1 of
492 adulthood expressing the secreted reporter *myo-3*p::ssGFP using Nexcope
493 microscopy. The average fluorescence intensity of the ssGFP signal was quantified
494 using ImageJ software. At least 18 animals were analyzed for each strain and condition.

495

496 **Quantification of NUC-1::pHTomato intensity**

497 Synchronized Day 1 adult *C. elegans* expressing P_{hs}NUC-1::pHTomato were first
498 subjected to a 33°C heat shock for 30 minutes to induce expression. Following
499 induction, animals were allowed to recover at 20°C for 24 hours before imaging[40,43].
500 The average intensity of pHTomato was then quantified per area in the hypodermis
501 using ImageJ software. A minimum of 20 worms were analyzed for each strain.

502

503 **Western blotting**

504 A total of 200 synchronized day 1 adult worms were collected, lysed directly in 1×
505 sample buffer, and boiled at 95°C for 10 minutes. The resulting protein extracts were
506 separated by SDS-polyacrylamide gel electrophoresis (SDS-PAGE) and transferred
507 onto a PVDF membrane. The membrane was blocked for 1 hour at room temperature
508 using 5% non-fat milk in TBST before being incubated overnight at 4°C with the
509 following primary antibodies: anti-GFP rabbit polyclonal antibody (1:1000, abclonal,
510 AE011), anti-α-tubulin mouse monoclonal antibody (1:5000, Sigma-Aldrich, T5168),
511 anti- flag DDDDK-tag mAb antibody (1:10000, MBL, M185) and anti-GAPDH antibody
512 (1:500, Absin, abs830030ss). After washing, the membrane was incubated with HRP-
513 conjugated secondary antibodies for 1 hour at room temperature. Finally, protein bands
514 were visualized using an enhanced chemiluminescence (ECL) detection system.

515

516 **Protein Sequence and Structure Prediction**

517 The protein sequences for human NCOA7 (NCBI accession: NP_001186548.1) and
518 its *C. elegans* ortholog LMD-3 (NCBI accession: NP_505173.2) were retrieved from
519 the National Center for Biotechnology Information (NCBI) database. Comparative
520 three-dimensional (3D) structural modeling for wild-type and the W690C mutant was
521 performed using. The predicted structures were visualized and analyzed using the
522 ChimeraX 1.10.1 software package.

523

524 **Inter-domain distance measurement**

525 To quantify the structural impact of the mutation on the predicted LMD-3 trimer-like
526 region, the distances between the conserved, and domains were measured. The
527 centroid of each respective domain was defined as a vertex of a triangle. The distances
528 between these centroids were then calculated using the “Distance” function within the
529 “Annotation” module of ChimeraX 1.10.1.

530

531 **Protein stability prediction**

532 To assess the effect of the point mutation on protein stability, we employed six distinct
533 machine learning-based prediction tools[51-55]. The LMD-3 protein sequence and 3D
534 structural model were the same as those used for the structural analysis above. For
535 each web-based tool, the W690C substitution was specified to calculate the change in
536 free energy (ΔΔG). The definition of a "Destabilizing" prediction varied among the
537 different websites, corresponding to specific ΔΔG thresholds.

538

539 **Statistical analysis**

540 All data were statistically analyzed using GraphPad Prism 9. Data are presented as
541 the mean, with error bars representing the standard error of the mean (SEM). Student’s
542 t-tests were utilized for comparisons between two distinct groups, while one-way

ANOVA tests were performed for multiple group comparisons. Statistical significance was established at $p < 0.05$ (indicated by *), $p < 0.01$ (indicated by **), and $p < 0.001$(indicated by ***).

Data availability

All data supporting the findings of this study, presented within the main manuscript and the Supplementary Information, are available in the accompanying Source data file provided with this paper. All unique reagents and strains generated throughout this study are available from the corresponding author upon reasonable request and the completion of a standard Material Transfer Agreement (MTA).

Acknowledgements

We thank the Caenorhabditis Genetics Center (CGC), Dr. Xiaochen Wang (Southern University of Science and Technology), Dr. Dengke Ma (UCSF), and Dr. Chenggang Zou (Yunnan University) for strains. Dr. Yingying Qin, Dr. Ting Dong, and Dr. Xue Jiao for their valuable suggestions (Shandong University).

Funding

This study was supported by a grant (no. 2022KF006 to Z.Z.) from YNCUB, the National Natural Science Foundation of China (32170781 to Z.Z.), and the Natural

Science Foundation of Shandong Province (2023HWYQ-014, tsqn202306056, ZR2021QC023, and 2021JK032 to Z.Z.).

Author contributions

Conceptualization: W.L, X.W, Z.Z; Data Curation: Y.Z, T.W, Z.Z; Formal Analysis: Y.Z, T.W; Funding Acquisition: Z.Z; Investigation: Y.Z, T.W, M.G, W.L, X.W, Z.Z; Methodology: Y.Z, T.W, M.G, W.L, Z.Z; Project Administration: Y.Z, T.W, W.L, X.W, Z.Z; Resources: T.W, M.G, Z.Z; Supervision: W.L, X.W, Z.Z; Validation: Y.Z, T.W, M.G, W.L; Visualization: Y.Z, T.W, M.W, Z.Z; Writing – Original Draft: Y.Z, T.W, M.W; Writing – Review & Editing: W.L, X.W, Z.Z.

Competing interests

The authors declare no competing interests.

References

1 Broekmans, F., Soules, M. & Fauser, B. Ovarian aging: mechanisms and clinical consequences. *Endocrine reviews* **30**, 465-493 (2009).

2 Scharf, A., Pohl, F., Egan, B. M., Kocsisova, Z. & Kornfeld, K. Reproductive aging in Caenorhabditis elegans: from molecules to ecology. *Frontiers in cell and developmental biology* **9**, 718522 (2021).

3 Benayoun, B. A., Kochersberger, A. & Garrison, J. L. Studying ovarian aging and its health impacts: modern tools and approaches. *Genes & Development* **39**, 975-990 (2025).

4 Te Velde, E. R. & Pearson, P. L. The variability of female reproductive ageing. *Human reproduction update* **8**, 141-154 (2002).

587 5 Park, S. U., Walsh, L. & Berkowitz, K. M. Mechanisms of ovarian aging.
588 *Reproduction* **162**, R19-R33 (2021).

589 6 Sala, A. J. & Morimoto, R. I. Protecting the future: balancing proteostasis for
590 reproduction. *Trends in cell biology* **32**, 202-215 (2022).

591 7 Agarwal, A., Gupta, S. & Sharma, R. K. Role of oxidative stress in female
592 reproduction. *Reproductive biology and endocrinology* **3**, 28 (2005).

593 8 Agarwal, A., Aponte-Mellado, A., Premkumar, B. J., Shaman, A. & Gupta, S. The
594 effects of oxidative stress on female reproduction: a review. *Reproductive biology*
595 *and endocrinology* **10**, 49 (2012).

596 9 Fredriksson, Å. *et al.* Effects of aging and reproduction on protein quality control
597 in soma and gametes of Drosophila melanogaster. *Aging cell* **11**, 634-643 (2012).

598 10 Ye, A. L. & Bhalla, N. Reproductive aging: insights from model organisms.
599 *Biochemical Society Transactions* **39**, 1770-1774 (2011).

600 11 Hughes, S. E., Evason, K., Xiong, C. & Kornfeld, K. Genetic and pharmacological
601 factors that influence reproductive aging in nematodes. *PLoS genetics* **3**, e25
602 (2007).

603 12 Zimmerman, S. M., Hinkson, I. V., Elias, J. E. & Kim, S. K. Reproductive aging
604 drives protein accumulation in the uterus and limits lifespan in C. elegans. *PLoS*
605 *genetics* **11**, e1005725 (2015).

606 13 Bohnert, K. A. & Kenyon, C. A lysosomal switch triggers proteostasis renewal in
607 the immortal C. elegans germ lineage. *Nature* **551**, 629-633 (2017).

608 14 Song, Z. *et al.* Germ cell-specific Atg7 knockout results in primary ovarian
609 insufficiency in female mice. *Cell death & disease* **6**, e1589-e1589 (2015).

610 15 Labbadia, J. & Morimoto, R. I. The biology of proteostasis in aging and disease.
611 *Annual review of biochemistry* **84**, 435-464 (2015).

612 16 Durand, M. *et al.* The OXR domain defines a conserved family of eukaryotic
613 oxidation resistance proteins. *BMC cell biology* **8**, 13 (2007).

614 17 Finelli, M. J. & Oliver, P. L. TLDc proteins: new players in the oxidative stress
615 response and neurological disease. *Mammalian Genome* **28**, 395-406 (2017).

616 18 Finelli, M. J., Sanchez-Pulido, L., Liu, K. X., Davies, K. E. & Oliver, P. L. The
617 evolutionarily conserved Tre2/Bub2/Cdc16 (TBC), lysin motif (LysM), domain
618 catalytic (TLDc) domain is neuroprotective against oxidative stress. *Journal of*
619 *Biological Chemistry* **291**, 2751-2763 (2016).

620 19 Dong, T. *et al.* Stress granule clearance mediated by V-ATPase-interacting protein
621 NCOA7 mitigates ovarian aging. *Nature Aging*, 1-20 (2025).

622 20 Sanada, Y. *et al.* Oxidation resistance 1 is essential for protection against oxidative
623 stress and participates in the regulation of aging in Caenorhabditis elegans. *Free*

radical research **48**, 919-928 (2014).

21 Xu, H. *et al.* Zebrafish Oxr1a knockout reveals its role in regulating antioxidant defenses and aging. *Genes* **11**, 1118 (2020).

22 Eaton, A. F., Brown, D. & Merkulova, M. The evolutionary conserved TLDc domain defines a new class of (H+) V-ATPase interacting proteins. *Scientific reports* **11**, 22654 (2021).

23 Oot, R. A. & Wilkens, S. Human V-ATPase function is positively and negatively regulated by TLDc proteins. *Structure* **32**, 989-1000. e1006 (2024).

24 Madeira, F. *et al.* The EMBL-EBI Job Dispatcher sequence analysis tools framework in 2024. *Nucleic acids research* **52**, W521-W525 (2024).

25 Waterhouse, A. M., Procter, J. B., Martin, D. M., Clamp, M. & Barton, G. J. Jalview Version 2—a multiple sequence alignment editor and analysis workbench. *Bioinformatics* **25**, 1189-1191 (2009).

26 Moriwaki, T., Kato, S., Kato, Y., Hosoki, A. & Zhang-Akiyama, Q.-M. Extension of lifespan and protection against oxidative stress by an antioxidant herb mixture complex (KPG-7) in Caenorhabditis elegans. *Journal of Clinical Biochemistry and Nutrition* **53**, 81-88 (2013).

27 Hayashi, Y. *et al.* Nutritional and metabolic control of germ cell fate through O-GlcNAc regulation. *EMBO reports* **24**, e56845 (2023).

28 Albert Hubbard, E. J. & Schedl, T. Biology of the Caenorhabditis elegans germline stem cell system. *Genetics* **213**, 1145-1188 (2019).

29 Kimble, J. & Seidel, H. C. elegans germline stem cells and their niche. *StemBook [Internet]* (2013).

30 Gartner, A., Boag, P. R. & Blackwell, T. K. Germline survival and apoptosis. *WormBook: The Online Review of C. elegans Biology [Internet]* (2018).

31 Wu, Y.-C., Wang, X. & Xue, D. Methods for studying programmed cell death in C. elegans. *Methods in Cell Biology* **107**, 295-320 (2012).

32 Li, X., Singh, N., Miller, C., Sosseh, B. & Gordon, K. L. The C. elegans gonadal sheath Sh1 cells extend asymmetrically over a differentiating germ cell population in the proliferative zone. *Elife* **11**, e75497 (2022).

33 Halachmi, S. *et al.* Estrogen receptor-associated proteins: possible mediators of hormone-induced transcription. *Science* **264**, 1455-1458 (1994).

34 Oliver, P. L. *et al.* Oxr1 is essential for protection against oxidative stress-induced neurodegeneration. *PLoS genetics* **7**, e1002338 (2011).

35 Elliott, N. A. & Volkert, M. R. Stress induction and mitochondrial localization of Oxr1 proteins in yeast and humans. *Molecular and cellular biology* **24**, 3180-3187 (2004).

36 Rong, B. *et al.* Ribosome 18S m6A methyltransferase METTL5 promotes translation initiation and breast cancer cell growth. *Cell reports* **33** (2020).

37 Higuchi-Sanabria, R. *et al.* Divergent nodes of non-autonomous UPRER signaling through serotonergic and dopaminergic neurons. *Cell reports* **33** (2020).

38 Kaushik, S. & Cuervo, A. M. Proteostasis and aging. *Nature medicine* **21**, 1406-1415 (2015).

39 Lo, C. H. & Zeng, J. Defective lysosomal acidification: a new prognostic marker and therapeutic target for neurodegenerative diseases. *Translational neurodegeneration* **12**, 29 (2023).

40 Wang, Z. *et al.* The RBG-1–RBG-2 complex modulates autophagy activity by regulating lysosomal biogenesis and function in C. elegans. *Journal of Cell Science* **132**, jcs234195 (2019).

41 Barral, D. C. *et al.* Current methods to analyze lysosome morphology, positioning, motility and function. *Traffic* **23**, 238-269 (2022).

42 Egami, Y., Taguchi, T., Maekawa, M., Arai, H. & Araki, N. Small GTPases and phosphoinositides in the regulatory mechanisms of macropinosome formation and maturation. *Frontiers in physiology* **5**, 374 (2014).

43 Sun, Y. *et al.* Lysosome activity is modulated by multiple longevity pathways and is important for lifespan extension in C. elegans. *elife* **9**, e55745 (2020).

44 Jia, K., Hart, A. C. & Levine, B. Autophagy genes protect against disease caused by polyglutamine expansion proteins in Caenorhabditis elegans. *Autophagy* **3**, 21-25 (2007).

45 Nakamura, S. *et al.* Mondo complexes regulate TFEB via TOR inhibition to promote longevity in response to gonadal signals. *Nature communications* **7**, 10944 (2016).

46 Chen, H.-D. *et al.* HLH-30/TFEB-mediated autophagy functions in a cell-autonomous manner for epithelium intrinsic cellular defense against bacterial pore-forming toxin in C. elegans. *Autophagy* **13**, 371-385 (2017).

47 Chang, J. T., Kumsta, C., Hellman, A. B., Adams, L. M. & Hansen, M. Spatiotemporal regulation of autophagy during Caenorhabditis elegans aging. *Elife* **6**, e18459 (2017).

48 Wu, F. *et al.* Structural basis of the differential function of the two C. elegans Atg8 homologs, LGG-1 and LGG-2, in autophagy. *Molecular cell* **60**, 914-929 (2015).

49 Wei, W. & Ruvkun, G. Lysosomal activity regulates Caenorhabditis elegans mitochondrial dynamics through vitamin B12 metabolism. *Proceedings of the National Academy of Sciences* **117**, 19970-19981 (2020).

50 Abramson, J. *et al.* Accurate structure prediction of biomolecular interactions with

AlphaFold 3. *Nature* **630**, 493-500 (2024).

51 Pires, D. E., Ascher, D. B. & Blundell, T. L. mCSM: predicting the effects of mutations in proteins using graph-based signatures. *Bioinformatics* **30**, 335-342 (2014).

52 Pandurangan, A. P., Ochoa-Montano, B., Ascher, D. B. & Blundell, T. L. SDM: a server for predicting effects of mutations on protein stability. *Nucleic acids research* **45**, W229-W235 (2017).

53 Pires, D. E., Ascher, D. B. & Blundell, T. L. DUET: a server for predicting effects of mutations on protein stability using an integrated computational approach. *Nucleic acids research* **42**, W314-W319 (2014).

54 Savojardo, C., Fariselli, P., Martelli, P. L. & Casadio, R. INPS-MD: a web server to predict stability of protein variants from sequence and structure. *Bioinformatics* **32**, 2542-2544 (2016).

55 Capriotti, E., Calabrese, R. & Casadio, R. Predicting the insurgence of human genetic diseases associated to single point protein mutations with support vector machines and evolutionary information. *Bioinformatics* **22**, 2729-2734 (2006).

56 Kao, S.-H. *et al.* Analysis of protein stability by the cycloheximide chase assay. *Bio-protocol* **5**, e1374-e1374 (2015).

57 Zhao, Q., Gao, S. M. & Wang, M. C. Molecular mechanisms of lysosome and nucleus communication. *Trends in biochemical sciences* **45**, 978-991 (2020).

58 Settembre, C. *et al.* A lysosome-to-nucleus signalling mechanism senses and regulates the lysosome via mTOR and TFEB. *The EMBO journal* **31**, 1095-1108 (2012).

59 Lamming, D. W. & Bar-Peled, L. Lysosome: The metabolic signaling hub. *Traffic* **20**, 27-38 (2019).

60 Jentoft, I. M. A. & Schuh, M. Protein Storage in Oocytes: Implications for Oocyte Quality, Embryonic Development, and Female Fertility. *Annual Review of Cell and Developmental Biology* **41** (2025).

61 López-Otín, C., Blasco, M. A., Partridge, L., Serrano, M. & Kroemer, G. Hallmarks of aging: An expanding universe. *Cell* **186**, 243-278 (2023).

62 Takahashi-Iñiguez, T., García-Hernandez, E., Arreguín-Espinosa, R. & Flores, M. E. Role of vitamin B12 on methylmalonyl-CoA mutase activity. *Journal of Zhejiang University Science B* **13**, 423-437 (2012).

63 Costanzo, M. *et al.* Methylmalonic acidemia triggers lysosomal-autophagy dysfunctions. *Cell & Bioscience* **14**, 63 (2024).

64 Touraine, P. *et al.* Premature ovarian insufficiency. *Nature Reviews Disease Primers* **10**, 63 (2024).

65 Bretou, M. *et al.* Lysosome signaling controls the migration of dendritic cells. *Science immunology* **2**, eaak9573 (2017).

66 Powers, E. T., Morimoto, R. I., Dillin, A., Kelly, J. W. & Balch, W. E. Biological and chemical approaches to diseases of proteostasis deficiency. *Annual review of biochemistry* **78**, 959-991 (2009).

67 Wang, M. C., Oakley, H. D., Carr, C. E., Sowa, J. N. & Ruvkun, G. Gene pathways that delay Caenorhabditis elegans reproductive senescence. *PLoS genetics* **10**, e1004752 (2014).

68 Pu, X. & Qi, B. Lysosomal dysfunction by inactivation of V-ATPase drives innate immune response in C. elegans. *Cell Reports* **43** (2024).

69 Liu, Y. *et al.* ALKBH1 promotes HIF-1 α-mediated glycolysis by inhibiting N-glycosylation of LAMP2A. *Cellular and Molecular Life Sciences* **81**, 130 (2024).

1 **Figures**

2 **Fig. 1**

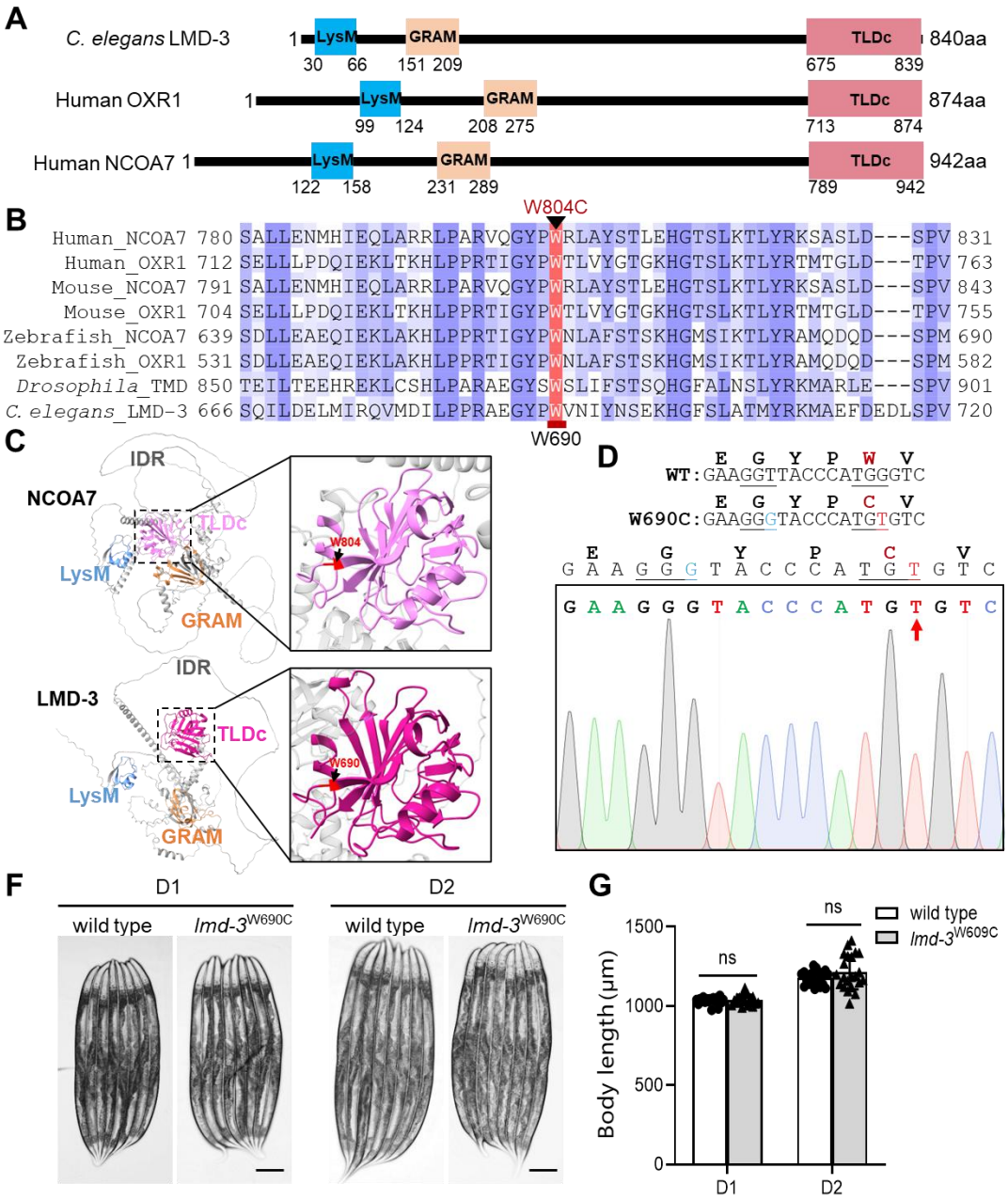

3 **Fig 1. Characterization of the POI-associated W690C Mutation in the conserved**

4 **TLDc domain of *C. elegans* LMD-3. A** Schematic representation of conserved

5 domains in *C. elegans* LMD-3 and its human orthologs, OXR1 and NCOA7. The

6 schematic diagrams illustrate the conserved LysM, GRAM, and TLDc domains. The

total number of amino acids (aa) is indicated for each protein. **B** The conserved tryptophan residue (W804) associated with premature ovarian insufficiency (POI) is highly conserved across species. A multiple sequence alignment of NCOA7 orthologs from five different species demonstrates the conservation of POI-associated W804 residue in human NCOA7. The residue, corresponding to W690 in *C. elegans* LMD-3, is highlighted with a red arrowhead. **C** Comparative structural analysis of the TLDc domain from human NCOA7 and *C. elegans* LMD-3. The TLDc domains are shown in detail to highlight their conserved structure similarity. The intrinsically disordered region (IDR) is colored gray. The conserved POI-associated tryptophan residues (human W804 and *C. elegans* W690) are indicated by black arrows and are colored red in the detailed view. **D** Sequencing confirmation of the *C. elegans lmd-3*^{W690C} knock-in allele. A representative DNA sequencing trace shows the successful creation of the POI-associated W690C mutation. A red arrow marks the target base change. The target knock-in site is indicated by a red arrow. The resulting amino acid change (W to C) is highlighted in red, while a silent mutation introduced for screening is highlighted in light blue. **F**, **G** Development defects detection between wild-type and *lmd-3*^{W690C} animals at D1 and D2 adult stages with bright-field image (**F**) and quantification (**G**) of animal body lengths (n ≥ 22 for each group, unpaired t-tests: ns, no significant difference). Scale bar, 50 μm.

26 **Fig. 2**

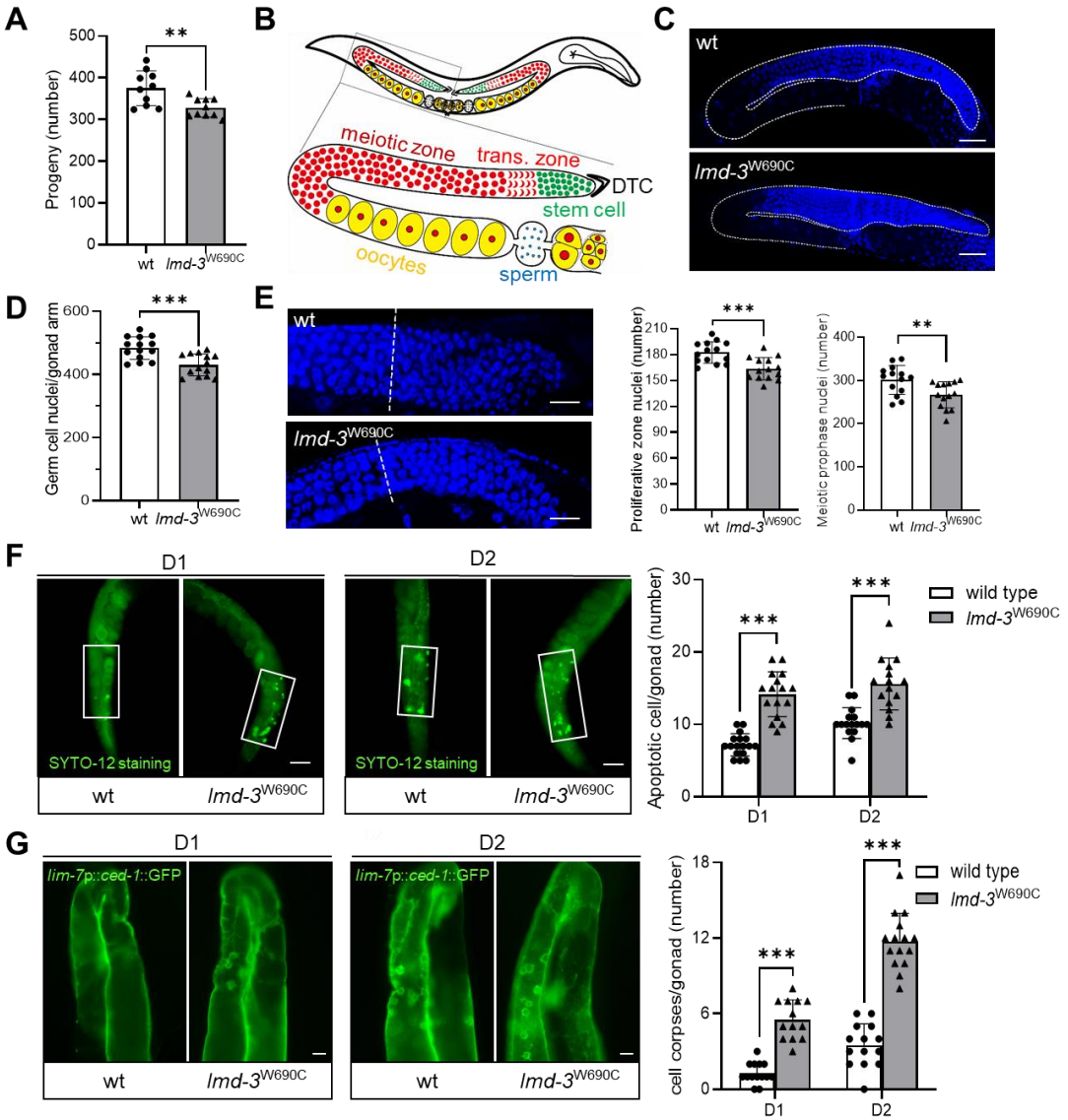

27 **Fig 2. The POI-associated W690C mutation in *C. elegans* LMD-3 impairs**

28 **fecundity and germline integrity. A** Total brood sizes indicate the overall

29 reproductive ability of wild-type and *lmd-3*^{W690C} mutants. Data are presented as mean

30 ± SEM (n = 10 per group, $^{**}p < 0.01$). **B** Spatial organization of the C. elegans germline

31 stem cell and meiotic regions. The schematic diagram illustrates one of the two distinct

32 gonad arms, showing the spatial organization of the stem cell region, transition zone,

33 and the meiotic phase along the distal-proximal axis. The distal tip cell (DTC) is also

depicted, highlighting its role in enclosing the distal arm. **C, D** Representative fluorescence images (**C**) and quantification (**D**) of DAPI-stained total germline cells in wild-type and *lmd-3*^{W690C} mutants (n = 14 for each group, ***$p < 0.001$). Scale bars, 50 μm. **D** Representative fluorescence images and quantification of DAPI staining for germline stem cells and meiotic cells in wild-type and *lmd-3*^{W690C} mutants (n = 14 for each group, **$p < 0.01$, ***$p < 0.001$). Scale bars, 20 μm. **F, G** Germline apoptosis in wild-type and *lmd-3*^{W690C} mutants with SYTO12 staining (**F**) and a *lim-7p::ced-1::GFP* reporter (**G**). White arrowheads indicate apoptotic cell corpses. n ≥ 13 per group; unpaired t-tests, ***$p < 0.001$. D1, Day 1 of adulthood; D2, Day 2 of adulthood. Scale bars, 50 μm.

44 **Fig. 3**

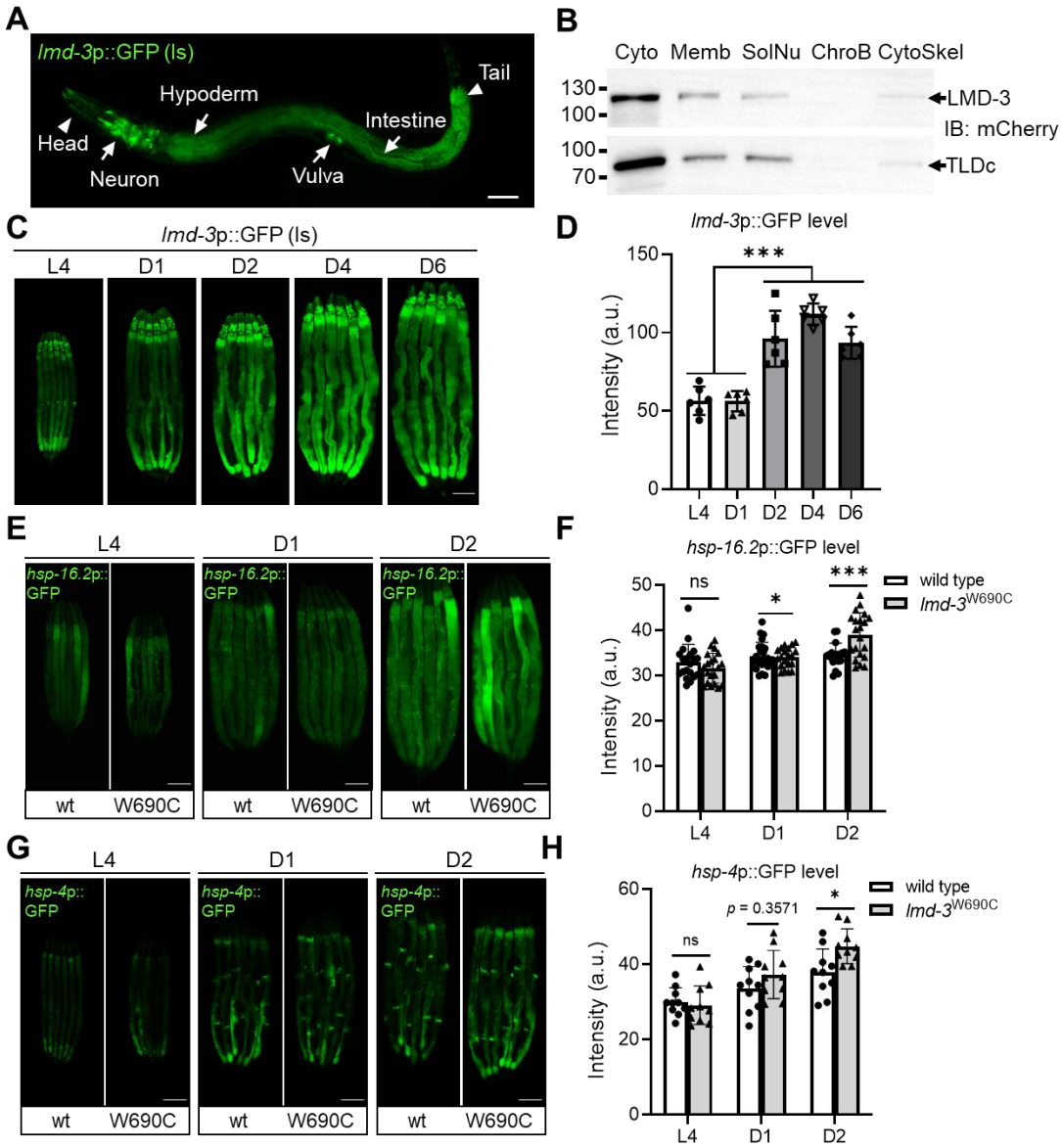

45 **Fig 3. The expression pattern of LMD-3 and the role of W690C mutation in stress**

46 **response. A** Expression pattern of *lmd-3* at the L4 larval stage. Representative images

47 show the expression of the *lmd-3p*::GFP transcriptional reporter). Is, integrated

48 transgene. Scale bars, 100 μm. **B** Subcellular localization of full-length LMD-3 and its

49 TLDc domain. The distribution of mCherry-tagged full-length LMD-3 (upper) and

50 mCherry-tagged TLDc domain (lower) was analyzed. The fractions analyzed were

51 cytoplasmic (Cyto), membrane (Memb), soluble nuclear (SolNu), chromatin-bound

52 (ChroB), and cytoskeletal (CytoSkel). **C, D** Transcriptional level of *lmd-3* during
53 different developmental stages with representative fluorescence images (**C**) and
54 quantification (**D**) using the *lmd-3*p::GFP reporters (n ≥ 6 for each group, ***$p < 0.001$).
55 Is, integrated transgene. Scale bars, 100 μm. a.u., arbitrary units. **E, F** Representative
56 fluorescence images (**E**) and quantification (**F**) of the UPR^{cyto} reporter *hsp-16.2*p::GFP
57 in wild type and *lmd-3*^{W690C} animals at indicated stages (n ≥ 20 for each group, ns, no
58 significant difference). Scale bars represent 100 μm. a.u., arbitrary units. L4, the fourth
59 larval stage. D1, Day 1 of adulthood. D2, Day 2 of adulthood. **G, H** Representative
60 fluorescence images (**G**) and quantification (**H**) of the UPR^{ER} reporter *hsp-*
61 *4*p::GFP in wild-type and *lmd-3*^{W690C} animals at indicated stages (n ≥ 10 for each
62 group, unpaired t-tests: ns, no significant difference, *$p < 0.05$). Scale bars
63 represent 100 μm. a.u., arbitrary units.

64 **Fig. 4**

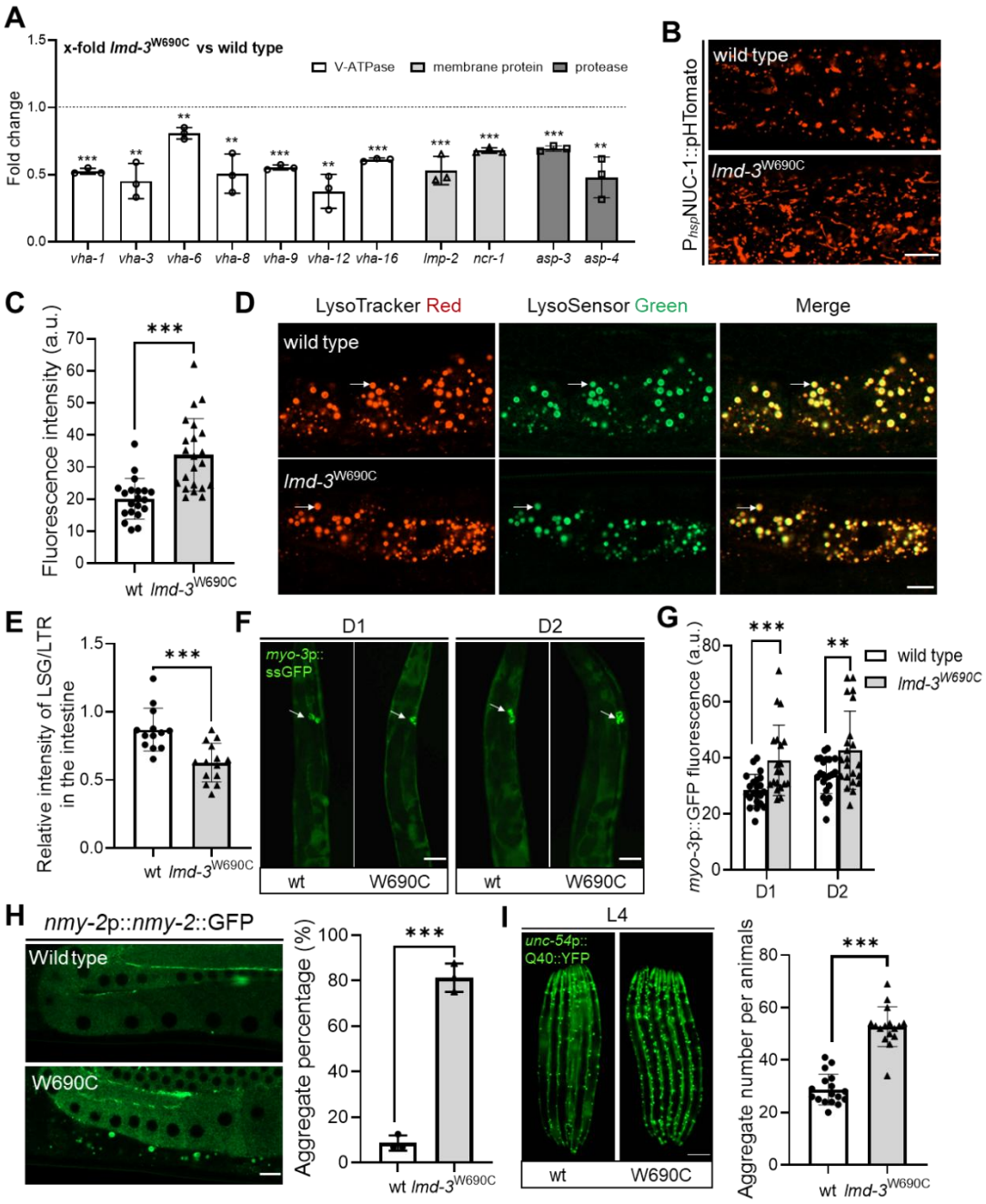

65 **Fig 4. The W690C mutation affects proteostasis and lysosomal function in *C.***

66 ***elegans*. A** Transcriptional analysis of lysosome-related genes in wild type and *lmd-*

67 *3*^{W690C} animals at the D1 adult stage (n = 3 for each group, unpaired t-tests: $^{**}p < 0.01$,

68 $^{***}p < 0.001$). **B, C** Representative fluorescence images (**B**) and quantification (**C**) of

69 NUC-1::pHTomato expression in the hypodermis driven by a heat-shock (hs) promoter

70 (n ≥ 20 per group, ***p < 0.001). a.u., arbitrary units. Scale bar, 10 μm. **D, E**
71 Representative confocal fluorescence images (**D**) and quantification (**E**) of intestines
72 co-stained with Lysosome-Specific Green (LSG DND-189) and Lysosome-Targeting
73 Red (LTR DND-99) in wild type and *lmd-3*^{W690C} animals at the D1 adult stage. White
74 arrowheads indicate vesicular lysosomes stained by both dyes. Relative intensity of
75 LSG/LTR were quantified (n ≥ 13 per group, ***p < 0.001). Scale bars, 10 μm. **F, G**
76 Representative fluorescence images (**F**) and quantification (**G**) of secreted protein
77 accumulation (*myo-3*p::ssGFP) in the coelomocytes of wild type and *lmd-3*^{W690C}
78 animals at the D1and D2 stages (n ≥ 18 per group, unpaired t-tests: **p < 0.01, ***p <
79 0.001). Scale bars, 50 μm. a.u., arbitrary units. **H** Confocal fluorescence images and
80 quantification of NMY-2::GFP accumulation in wild type and *lmd-3*^{W690C} animals at D1
81 stage (mean ± SEM, n = 3 biological replicates, 10 animals per condition per replicate,
82 unpaired t-tests: ***p < 0.001). **I** Fluorescence images and quantification of Q40::YFP
83 accumulation in the body wall muscles in wild type and *lmd-3*^{W690C} animals at the L4
84 stage (n ≥ 16 per group, unpaired t-tests: ***p < 0.001). Scale bars, 50 μm.

85 **Fig. 5**

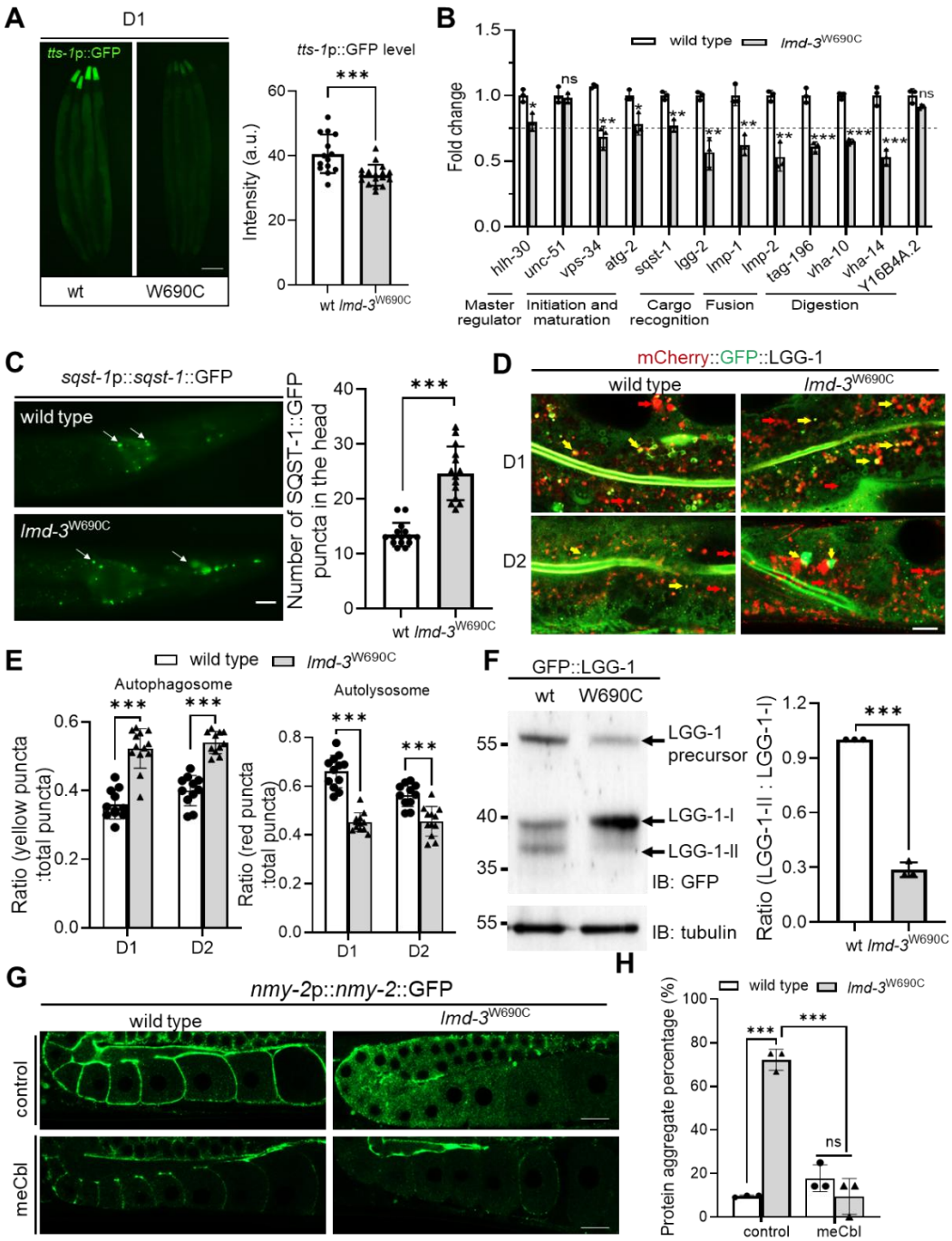

86 **Fig 5. meCbl restores proteostasis in LMD-3(W690C) mutants by repairing**

87 **autophagic-lysosomal defects. A** Representative fluorescence images and

88 quantification of the autophagy reporter *tts-1*p::GFP in wild type and *lmd-3*^{W690C} animals

89 at the indicated stages (n ≥ 10 per group, ***$p < 0.001$). a.u., arbitrary units. Scale bars

90 represent 100 μm. **B** Transcriptional analysis of key autophagy genes was performed
91 in wild type and *lmd-3*^{W690C} animals, and gene expression was quantified by RT-qPCR
92 (n = 3 per group, unpaired t-tests: *$p < 0.05$, **$p < 0.01$, ***$p < 0.001$, ns, no significant
93 difference). **C** Representative fluorescence images and quantification of SQST-1::GFP
94 accumulation in wild type and *lmd-3*^{W690C} animals at D1 adult stage (n ≥ 14 per group,
95 ***$p < 0.001$). White arrowheads denote fluorescent protein aggregates. Scale bars,
96 50 μm. **D, E** Representative confocal images (**D**) and quantification (**E**) of the
97 mCherry::GFP::LGG-1 reporter in wild type and *lmd-3*^{W690C} animals at D1 and D2 adult
98 stages. The ratio of autophagosomes (yellow puncta, yellow arrow) to total puncta and
99 autolysosomes (red puncta, red arrow) to total puncta was quantified (n ≥ 11 per group,
100 ***$p < 0.001$). Scale bar, 10 μm. **F** Representative Western blot and corresponding
101 quantification of the ratio of lipidated LGG-1-II to unlipidated LGG-1-I protein in wild-
102 type and *lmd-3*^{W690C} mutant animals (n = 3 biological replicates, ***$p < 0.001$). a.u.,
103 arbitrary units. IB, immunoblotting. **G, H** Confocal fluorescence images (**G**) and
104 corresponding quantification (**H**) of *nmy-2*p::*nmy-2*::GFP accumulation in the oocytes
105 of wild-type and *lmd-3*^{W690C} mutants at D1 of adulthood, with mecobalamin (meCbl)
106 supplementation (mean ± SEM, n=3 biological replicates, animals per condition per
107 replicate = 10, ***$p < 0.001$, ns, no significant differences). Scale bars, 10 μm.

108 **Fig. 6**

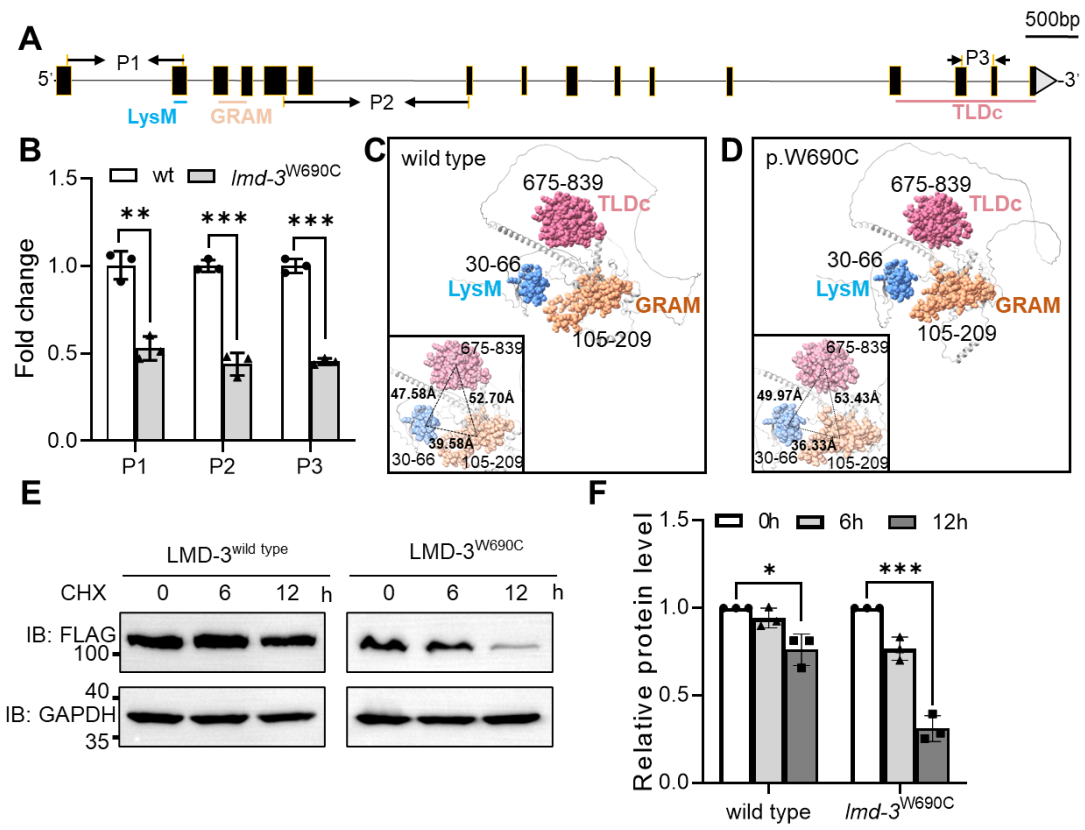

109 **Fig 6. The W690C mutation affects LMD-3 protein structure and stability. A** The
110 schematic diagram shows the genomic structure of *lmd-3*, including the positions of its
111 conserved LysM, GRAM, and TLDc domains. The locations of the qRT-PCR primers
112 (P1, P2, P3) designed to quantify lmd-3 mRNA are also shown. **B** qRT-PCR
113 measurements for endogenous *lmd-3* mRNA levels in wild type (wt) and *lmd-*
114 *3*^{W690C}animals (n = 3 per group, unpaired t-tests: $^{**}p < 0.01$, $^{***}p < 0.001$). **C, D**
115 Structural analysis of the LMD-3^{W690C} protein. Predicted three-dimensional structures
116 of wild-type (**C**) and W690C (**D**) proteins are presented to illustrate the effects of the
117 W690C mutation on protein folding. Key domains are color-coded: LysM (cornflower
118 blue), GRAM (light salmon), and TLDc (pale violet red). A magnified view shows the

trimer-like region, where the mutation leads to altered inter-subunit distances in the p.W690C protein (49.97 Å, 53.43 Å, 36.33 Å) compared to the wild-type (47.58 Å, 52.70 Å, 39.58 Å). **E, F** The W690C mutation reduces LMD-3 protein stability. Western blot images (**E**) and semi-quantitative analysis (**F**) show the turnover of 1xFLAG-tagged LMD-3 in H293T cells treated with cycloheximide (CHX) for 0, 6, and 12 h (n = 3 biological replicates, *$p < 0.5$, ***$p < 0.001$). a.u., arbitrary units.